J. Phys. Chem. A
December 28, 2014
Harding, Michael, Wagner Festschrift

Multidimensional effects in nonadiabatic statistical theories of spin-forbidden kinetics

Ahren W. Jasper*

Combustion Research Facility, Sandia National Laboratories, Livermore, CA 94551, USA

Abstract

The appropriateness of treating crossing seams of electronic states of different spins as "nonadiabatic transition states" in statistical calculations of spin-forbidden reaction rates is considered. We show that the spin-forbidden reaction coordinate—the nuclear coordinate perpendicular to the crossing seam—is coupled to the remaining nuclear degrees of freedom. This coupling gives rise to multidimensional effects that are not typically included in statistical treatments of spin-forbidden kinetics. Three categories of multidimensional effects are identified: *static* multidimensional effects due to the geometry-dependence of the local shape of the crossing seam and of the spin-orbit coupling, *dynamical* multidimensional effects due to energy exchange with the reaction coordinate during the seam crossing, and *nonlocal* (history-dependent) multidimensional effects due to interference of the electronic variables at 2nd, 3rd, and later seam crossings. Nonlocal multidimensional effects are intimately related to electronic decoherence, where electronic dephasing acts to erase the history of the system. A semiclassical model based on short-time full-dimensional trajectories that includes all three multidimensional effects as well as a model for electronic decoherence is presented. The results of this multidimensional nonadiabatic statistical theory (MNST) for the $^3O + CO \rightarrow CO_2$ reaction are compared with the results of statistical theories employing one-dimensional (Landau-Zener and "weak coupling") models for the transition probability and with those calculated previously using multistate trajectories. The MNST method is shown to accurately reproduce the multistate decay-of-mixing trajectory results, so long as consistent thresholds are used. The MNST approach has several advantages over multistate trajectory approaches and is more suitable in chemical kinetics calculations at low temperatures and for complex systems. The error in statistical calculations that neglect multidimensional effects is shown to be as large as a factor of two for this system, with static multidimensional effects identified as the largest source of error.

Keywords: intersystem crossing, non-adiabatic transition state theory, NA TST, RRKM, classical path, semiclassical

*Electronic mail: ajasper@sandia.gov

I. Introduction

Several statistical treatments of spin-forbidden (and, more generally, electronically nonadiabatic or non-Born–Oppenheimer) kinetics have been proposed.[1,2,3,4,5,6,7,8,9,10,11,12] These methods differ from one another in their details but often make an analogy with (electronically adiabatic) transition state theory (TST). In 1937, Wigner had already noted the relationship between a saddle point on a single potential energy surface and the avoided crossing of two adiabatic potential energy surfaces.[13] More generally, nonadiabatic transitions can often be associated with seams of diabatic surface crossings, which have the same dimensionality as transition state dividing surfaces. For weakly coupled spin-forbidden reactions, such as those involving first-row atoms, electronic transitions are typically localized very tightly near the crossing seam, and TST-like theories quantifying the rate of access to the crossing seam would appear appropriate. While TST has been developed and applied with great success in the nine decades since its formulation,[14] statistical methods for electronically nonadiabatic processes have not been as widely advanced. Here, we critically evaluate nonadiabatic statistical theories, which typically employ one-nuclear-dimensional models for the nonadiabatic transition probability, and develop a multidimensional nonadiabatic statistical theory. The present approach is motivated in part by the theoretical limitations of treating the crossing seam as a "nonadiabatic transition state."

Wigner's defining assumption[13,15] of TST may be written: there exists a transition state dividing surface separating reactants from products constructed such that every system that reaches it does so only once and reacts with unit probability and no reactive system does not reach it. This assumption leads both to the formal proofs of the exactness of classical TST[16,17] and to practical variational theories[18] in which recrossing is minimized with respect to geometrical parameters of the dividing surface to improve the predicted reaction rate. TST is therefore a localized dynamical theory, requiring a detailed characterization of the N–1-dimensional transition state dividing surface, where

N is the number of internal degrees of the system, but not requiring global or time-dependent dynamics.

TST is formally a classical theory and does not naturally include quantum effects such as quantized vibrations, tunneling, nonadiabatic transitions, etc. Tunneling clearly violates the fundamental assumption of TST, allowing some reaction "ahead" of the transition state dividing surface and preventing some reaction at the transition state dividing surface due to nonclassical reflection. This situation is represented by the energy-dependent reaction probability for semiclassical tunneling shown in Fig. 1, where it is compared with classical TST's step-function reaction probability. Tunneling's blurring of the classical reaction probability near the transition state allows for coupling of the reaction coordinate to the other degrees of freedom[19]—tunneling may proceed via "corner cutting" paths,[20,21] for example. Semiclassical theories of tunneling that recognize the importance of multidimensional effects have been successfully incorporated into TST and widely applied.[22,23,24]

Figure 1 also shows a representative reaction probability for a weakly coupled spin-forbidden reaction as a function of the energy perpendicular to the crossing seam. Clearly the fundamental assumption of TST is not satisfied for this model and—unlike for semiclassical tunneling models—not even approximately so. Because the spin-forbidden transition probability is not a step function, one may anticipate *dynamical* multidimensional effects associated with nonseparability of the reaction coordinate, analogous to those that have been identified for tunneling.

Furthermore, the magnitude of the spin-forbidden reaction probability generally depends on the shapes of the interacting surfaces and on the spin–orbit coupling strength. If these are strong functions of geometry along the crossing seam, another multidimensional effect is introduced. This second multidimensional effect depends only on properties of the potential energy surfaces and their couplings, and so this may be labeled a nondynamical or *static* multidimensional effect.

Finally, the spin-forbidden reaction probability for weakly coupled systems does not approach unity at any energy. Access to the seam is therefore never the dynamical bottleneck for such reactions, although it can be required. Instead, the system may encounter the crossing seam many times without reacting, and multiple seam crossings may be required for appreciable overall reaction rates. The spin-forbidden transition probabilities at the 2^{nd}, 3^{rd}, and later seam crossings will depend on the entire history of the electronic variables at earlier crossings and on the intermediate nuclear dynamics. In polyatomic systems, later seam crossings will occur at geometries that are not related to the geometries of earlier seam crossings in any simple way, thus representing *nonlocal* multidimensional effects. This third multidimensional effect is related to electronic decoherence.[25] If the timescale for electronic decoherence is short relative to the time between seam encounters, the electronic variables may be expected to "reset" between seam encounters, which may then be treated independently. If not, more complicated theories are required. Interference of the electronic variables at multiple seam crossings occurs in one-dimension, as well, and so nonlocal effects are not strictly multidimensional. While analytic one-dimensional models for multiple coherent seam crossings have been developed,[26,27,28] their generalization to multidimensional systems is not straightforward.

The principal goals of the present work are (1) to critically evaluate the importance of dynamical, static, and nonlocal multidimensional effects in the spin-forbidden kinetics of $^3O + CO \rightarrow CO_2$, and (2) to present and apply a multidimensional nonadiabatic statistical theory suitable for practical kinetics calculations. This reaction has been identified as important in some combustion systems,[29] and its spin-forbidden kinetics have been studied theoretically via explorations of the coupled potential energy surfaces and via multistate semiclassical trajectories.[30,31,32] The $^3O + CO \rightarrow CO_2$ system is isoelectronic with $^3O + N_2 \rightarrow N_2O$, which was the subject of several of the earliest polyatomic nonadiabatic statistical theory studies.[1,2,3,4,5]

This paper is organized as follows. In Sec. II.A, existing statistical theories for spin-forbidden kinetics are reviewed, and this discussion is used to motivate the development of the multidimensional nonadiabatic statistical theory (MNST) presented in Sec. II.B. Section II.C summarizes the previously developed[32] diabatic representation of the CO_2 system that is used here. In Sec. III.A, spin-forbidden transition probabilities for one-dimensional model systems are obtained, and these are used as references for quantifying multidimensional effects in the full-dimensional calculations reported in Sec. III.B. Finally, in Sec. III.C, thermal MNST rate coefficients are reported and shown to agree with the results of an earlier multistate trajectory study[32] that employed the coherent switches with decay of mixing[33] (CSDM) method. Section IV is a summary.

II. THEORY

II.A. Summary of existing nonadiabatic statistical theories

Harvey reviewed[12] an approach for spin-forbidden kinetics calculations,[8,9] which, following earlier work,[3] has been called "nonadiabatic transition state theory." The rate expressions have a form similar to that of conventional TST (or RRKM) theory, but with a hopping coordinate replacing the usual reaction coordinate and a crossing seam replacing the usual transition state dividing surface. In a particularly useful version of this approach, the minimum-energy geometry on the crossing seam (MSX) is located, and harmonic frequencies locally perpendicular to the hopping coordinate are calculated.[34,35] The state count for the crossing seam is approximated using the rigid rotor and harmonic oscillator (RRHO) approximations. This approach is entirely analogous to the common approach of using RRHO state counts based on quadratic expansions about saddle points in TST. The nonadiabatic reactive flux is proportional to an effective nonadiabatic state count at the crossing seam N^*, which is obtained by convolving the RRHO state densities for the seam's degrees of freedom ρ with a nonadiabatic transition probability P, i.e.,

$$N^*(E) = \int dE' \rho(E - E') P(E') , \tag{1}$$

where we have neglected angular momentum in eq 1 to simplify our notation. Other workers have used TST-like expressions for nonadiabatic kinetics based on Monte Carlo integration of the crossing seam that avoid the RRHO approximation for ρ.[2,4,5,6,10] In either formulation, when P is replaced by the "classical TST" step function shown in Fig. 1, the methods reduce to the usual harmonic or anharmonic TST expressions.

For weakly coupled spin-forbidden reactions, P is not close to unity and is instead very small, where here P has been defined as the probability of switching diabatic surfaces. A widely used model for P is the Landau-Zener (LZ) model,[36,37] where

$$P_{\mathrm{LZ}}(E_\perp) = 1 - \exp\left(\frac{-2\pi H_{\mathrm{SO}}^2}{\hbar\left|\Delta F\right| v_\perp}\right), \tag{2}$$

$E_\perp$ is the energy in the hopping coordinate perpendicular to the crossing seam, H_{SO} is the spin–orbit coupling strength, $\left|\Delta F\right|$ is the norm of the gradient of the diabatic gap at the crossing seam in coordinates mass-scaled to μ, and $v_\perp = \sqrt{2E_\perp / \mu}$.

Equation 2 was obtained by considering a one-dimensional system with linear diabatic potentials and a constant diabatic coupling; the LZ model therefore cannot account for dynamical multidimensional effects. Likewise, the LZ model does not include any electronic phase information, and so nonlocal multidimensional effects cannot be studied with this model. Static multidimensional effects do arise in eq 2 via the geometry dependence of H_{SO} and $\left|\Delta F\right|$; this effect has been included in trajectory studies (for example[5,38]), most often only via $\left|\Delta F\right|$, however, with H_{SO} set to a constant value.

One could incorporate static multidimensional effects into eq 1 by setting $P = \langle P_{\mathrm{LZ}} \rangle_{\mathbf{R}}$, where the bracket denotes some appropriate (e.g., microcanonical) weighted average of P_{LZ} over the geometries on the crossing seam **R**, although we are not aware of any such studies. The incorporation of static multidimensional effects arises more naturally in Monte Carlo-based formulations for N*; studies of this type have typically been limited to three-atom systems with two-dimensional seams,[2,4,5] with the notable

exception of Marks' study of bromoacetylchloride.[10] An efficient strategy for sampling higher-dimensional seams has been reported.[39] In many calculations, the geometry-dependence of eq 2 is neglected, and P_{LZ} is instead evaluated at a reference geometry—for example the MSX. Comparing kinetics obtained via eq 1 and using either $P = \langle P_{LZ} \rangle_{\mathbf{R}}$ or $P = P_{LZ}$ evaluated at the MSX (denoted here P_{LZ}^{MSX}) is one means of quantifying static multidimensional effects.

Delos considered the one-dimensional dynamics of a nonadiabatic atom–atom association reaction[26] and recognized that one should not use P_{LZ} for each atom–atom collision, as the system will generally encounter the crossing seam twice: once as the two atoms come together and again as they separate. Each encounter with the crossing seam provides an opportunity for an electronic transition, and, at the second encounter, the population of the initially prepared electronic state has been depleted by the first encounter with the crossing seam. Delos suggested a "double passage" formula to incorporate these effects, where

$$P_{2LZ}(E_\perp) = P_{LZ} + (1 - P_{LZ})P_{LZ}. \tag{3}$$

Marks and Thompson provided an alternative double passage formula for systems with large transition probabilities.[4]

While eq 3 may be appropriate for some one-dimensional systems, its accuracy in spin-forbidden statistical calculations of polyatomic systems is not clear. Specifically, there is no guarantee in polyatomic systems that the system will encounter the crossing seam exactly twice during a single collision, and multiple encounters are not expected to occur at the same location on the crossing seam or with the same value of $E_\perp$.

For weakly coupled systems, we may generalize the "double passage" prescription for use in polyatomic statistical calculations as follows. First, we recognize that encountering the crossing seam from either side can lead to nonadiabatic transitions. This is in contrast to the TST expression, where only the one-way reactive flux is counted. (This arises in some derivations of TST, for example, by restricting the integral

over the reaction coordinate's momentum to positive values.[16]) The usual TST expressions should then be multiplied by 2 when used in the context of nonadiabatic dynamics. It is convenient to incorporate this factor of 2 into the nonadiabatic probability itself, particularly for large P, but its physical origin is as a correction for "two way" passage through the seam. Second, the nonadiabatic transition probability should include some average of first ($P_{\mathrm{LZ}}^{(1)} = P_{\mathrm{LZ}}$), second ($P_{\mathrm{LZ}}^{(2)} = (1 - P_{\mathrm{LZ}}^{(1)})P_{\mathrm{LZ}}$), and higher-order crossing probabilities, each with different dependencies on $E_{\perp}$, weighted by their relative likelihoods, e.g.,

$$P_{\mathrm{GLZ}}(E_{\perp}) = 2\sum_n w_n P_{\mathrm{LZ}}^{(n)} / \sum_n w_n \,, \tag{4}$$

where n = 1, 2, … labels the sets of 1st, 2nd, … seam crossings, etc., for ensembles of collisions. Generally, w_n and $P_{\mathrm{LZ}}^{(n)}$ will not be known and cannot be readily computed without a dynamical model. If, as in Delos' diatomic system, the first and second crossings are equally probable and there are no higher-order crossings, eq 4 reduces to eq 3. For small P_{LZ}, both eqs 3 and 4 are approximately equal to 2 P_{LZ}, which incorporates the required two-way correction to the TST equations for use in nonadiabatic theories but neglects the small effects of depletion.

The LZ model may be further criticized for weakly coupled systems. While the LZ model, by construction, tends to the adiabatic limit at low energies ($P_{\mathrm{LZ}}(0) = 1$), the nonadiabatic transition probability for a weakly-coupled one-dimensional system should instead tend to a small finite value,[27] which itself tends to zero as H_{SO}^2. An analytic weak coupling (WC) formula more appropriate for this limit has been given as[26,27,28]

$$P_{\mathrm{WC}}(E_{\perp}) = \pi^2 \beta^{4/3} \mathrm{Ai}^2(-\varepsilon\beta^{2/3}) \,, \tag{5}$$

where Ai is the Airy function,

$$\beta = \frac{4H_{\mathrm{SO}}}{\hbar}\sqrt{\frac{\mu H_{\mathrm{SO}}}{\bar{F}|\Delta F|}} \,, \tag{6}$$

$$\varepsilon = \frac{E_\perp |\Delta F|}{2H_{SO}\bar{F}}, \tag{7}$$

$$\bar{F} = \sqrt{|F_1 F_2|}, \tag{8}$$

and $F_i = -dV_i / ds$ is the gradient of the i^{th} diabatic surface along the hopping coordinate s (perpendicular to the crossing seam). Equation 5 is a "double passage" expression, i.e., it is the total transition probability for both passages through the crossing point obtained via a first-order approximation to the quantum mechanical solution in one-dimensional. Like the LZ formula, the one-dimensional WC formula cannot be used to study dynamical multidimensional effects, and static multidimensional effects can be studied via the geometry-dependence of H_{SO}, $\bar{F}$, and ΔF. Nonlocal phase interference effects in one-dimension are explicitly included in this model.

The WC formula includes the correct one-dimensional quantum mechanical weak coupling behavior at small $E_\perp$, including tunneling for $E_\perp < 0$ and interference of the electronic variables at the incoming and outgoing seam crossings.[28] The WC formula is defined for a pair seam crossings, and in particular for two seam crossings that occur at the same geometry and with a time interval estimated based on the geometric average of the gradients of the two surfaces at the crossing seam (eq 8). The appropriateness of this description of nonlocal effects in multidimensional applications is not clear, as there is no guarantee that the system will promptly return to the crossing seam, even at low $E_\perp$, and, if the system does return, subsequent crossings will generally occur at different locations on the crossing seam with different values of H_{SO}, $\bar{F}$, and ΔF.

In the WC model, the nonadiabatic dynamics depends only on the properties of the crossing seam and is independent of which electronic state is currently occupied. We may define an improved WC formula (IWC) that does depend on the occupied electronic state α, where, instead of the geometric mean given in eq 8, $\bar{F}$ is defined

$$\bar{F} = |F_\alpha|. \tag{9}$$

The IWC model may be more appropriate for weakly coupled systems where the reactants are initially prepared in a single electronic state and where the electronic population transferred during a single seam encounter is small. Equations 8 and 9 are generalized as $\bar{F} = \left| F_1^{n_1} F_2^{n_2} \right|$, where n_i is the electronic state population of state i, but such a model is not used here.

II.B. Multidimensional nonadiabatic statistical theory

Multidimensional nonadiabatic transition probabilities were computed semiclassically by solving the time-dependent Schrödinger equation for the electronic variables in the time-dependent field created by a moving classical trajectory, $\vec{R}(t)$. In the diabatic representation and for a two-state system, the coherent evolution of the complex-valued electronic state amplitudes, c_i, is given by[40,41]

$$\dot{c}_1 = -i\hbar^{-1}(c_1 V_1(\vec{R}(t)) + c_2 H_{SO}(\vec{R}(t)))$$

$$\dot{c}_2 = -i\hbar^{-1}(c_2 V_2(\vec{R}(t)) + c_1 H_{SO}(\vec{R}(t))), \qquad (10)$$

which are sometimes labeled "classical path" (CP) equations, where the diabatic potential energy surfaces and their coupling surface are labeled V_i and H_{SO}, respectively. The trajectories $\vec{R}(t)$ were obtained by sampling geometries and momenta on the crossing seam from an appropriate ensemble and initiating each trajectory such that it crossed the seam at the sampled point in phase space. Trajectories were propagated on a single diabatic electronic surface with no surface switches ("hops") allowed. Along each trajectory, the electronic state populations $n_i = c_i^* c_i$ were propagated via eq 10.

For weakly coupled systems, the transfer of electronic population is localized near the crossing seam. After passage through the seam and away from it, there is no longer any net transfer of electronic population, but the electronic state populations do undergo small-amplitude oscillations. The multidimensional classical path nonadiabatic transition probability P_{CP} for each passage through the crossing seam was calculated by averaging

in time over these oscillations. Specifically, for each seam crossing, the time along the trajectory when the diabatic surfaces crossed was denoted t_X, and the time chosen as the end of the associated nonadiabatic interaction, t_+, was defined (as in the CSDM method[33] and as suggested by Parlant and Gislason[42]) by the next local minimum in the magnitude of the nonadiabatic coupling vector[40] for the two interacting states; P_{CP} was then calculated as

$$P_{CP}(E_\perp, E) = \frac{1}{t_+ - t_-} \int_{t=t_-}^{t_+} dt\,(1 - n_\alpha(t))\,, \tag{11}$$

where t_- is halfway between t_X and t_+, and α is the occupied electronic state. Other simple rules for obtaining P_{CP} (such as setting $t_- = \frac{3}{4}\,(t_+ + t_X)$) gave very similar results.

Because the trajectories $\bar{R}(t)$ in eq 10 are full-dimensional, the associated CP nonadiabatic transition probabilities will generally depend both on the energy perpendicular to the crossing seam $E_\perp$ as well as on how the rest of the energy is distributed among the other degrees of freedom. Here we have made no attempt to resolve mode-specific details of P_{CP} and instead have considered P_{CP} as a function of $E_\perp$ and of the total internal energy E, as indicated in eq 11. The dependence of P_{CP} on E can be used to quantify dynamical multidimensional effects in this semiclassical model. Static multidimensional effects in P_{CP} arise via the **R**-dependence of the diabatic surfaces and couplings in eq 10. The complex-valued amplitudes c_i include electronic phase information, and nonlocal multidimensional effects are therefore also included in this model.

The total nonadiabatic transition probability for multiple coherent seam crossings, P_{2CP}, P_{3CP}, etc., may be calculated as in eq 11, with t_+ and t_- defined relative to the time of later seam crossings. The nonadiabatic transition probability associated with the 2nd seam crossing, e.g., is then $P_{CP}^{(2)} = P_{2CP} - P_{CP}^{(1)}$, where $P_{CP}^{(1)} \equiv P_{CP}$ is the nonadiabatic transition probability for the first seam crossing for the same trajectory. Note that $P_{CP}^{(n)}$ for

$n \geq 2$ is not guaranteed to be positive, and, more generally, the distribution of $P_{\mathrm{CP}}^{(n)}$ for $n \geq 2$ may differ from that of $P_{\mathrm{CP}}^{(1)}$. Furthermore, the energy in the hopping coordinate at the second crossing need not be equal to that at the first, i.e., $E_{\perp}^{(1)} \neq E_{\perp}^{(2)}$. The incorporation of these nonlocal multidimensional effects into statistical models of the type in eq 1 is not straightforward. The effect of electronic decoherence considerably improves the situation, as discussed next.

A decoherence event (i.e., the loss of electronic phase information) may be modeled semiclassically by resetting the electronic variables[33,43,44,45,46,47]—either instantaneously or over some short de-mixing time. In the present context, such a deocoherence event between seam encounters decouples the electronic dynamics at subsequent seam crossings. This effect was included in our model as follows: A characteristic decoherence time, τ_{d}, at each seam encounter was calculated via a previously described semiclassical approximation[48] based on the instantaneous dephasing of one-dimensional wave packets prepared in each of the two electronic states. At the end of each time step *dt* of the trajectory and starting only after the first seam crossing, decoherence events were modeled as occurring with a probability $1-\exp(-dt/\tau_{\mathrm{d}})$. When a decoherence event was called for, the trajectory was either stopped immediately or stopped after propagation to the next minimum in the magnitude of the nonadiabatic coupling vector, such that $P_{\mathrm{CP}}^{(n)}$ for all *n* prior seam encounters could be calculated via eq 11. This implementation is similar to the "stochastic decoherence" approach previously suggested for surface hopping trajectories.[44,49]

The trajectory ensembles described above, including the model for decoherence, were used to calculate $<P_{\mathrm{CP}}^{(n)}>_{\mathbf{R}}$ as well as the relative likelihood of a decoherence event occurring after the n^{th} seam crossing, w_n. The multidimensional nonadiabatic (MN) transition probability suitable for inclusion in a statistical calculation was then defined similarly to eq 4,

$$P_{\mathrm{MN}}(E_{\perp},E) = 2\sum_n w_n < P_{\mathrm{CP}}^{(n)} >_{\mathbf{R}} / \sum_n w_n \,. \tag{12}$$

The brackets in eq 12 include averaging over locations on the crossing seam and over how the total energy is distributed among the degrees of freedom during the nonadiabatic events.

The timescale for electronic decoherence τ_{d} is often expected to be very short; τ_{d} was previously calculated for CO_2 to be only a few fs.[30] In the limit of fast decoherence, $w_1 \approx 1$, which is equivalent in the present model to assuming $< P_{\mathrm{CP}}^{(n)} >_{\mathbf{R}} \approx < P_{\mathrm{CP}} >_{\mathbf{R}}$ for all n and that correlations between $E_{\perp}^{(n)}$ at subsequent seam crossings need not be considered. In this limit, eq 12 simplifies to

$$P_{\mathrm{MN}}(E_{\perp},E) \approx 2 < P_{\mathrm{CP}} >_{\mathbf{R}} , \tag{13}$$

which may be calculated by considering only "first passage" trajectories. The inclusion of (fast) decoherence thus simplifies the present calculations considerably. Trajectories required for evaluating P_{CP} for a single passage through the crossing seam were typically very short (<20 fs), whereas full trajectories (propagated from reactants to products) would have required on the order of 1 ps for this system.

Finally, the multidimensional nonadiabatic statistical theory (MNST) flux through the crossing seam was defined as in eq 1 but with the E-dependence of P_{MN} explicitly indicated,

$$N^{*}_{\mathrm{MNST}}(E) = \int dE' \rho(E - E') P_{\mathrm{MN}}(E', E) \,. \tag{14}$$

In the present applications, the rigid rotor and quantum mechanical harmonic oscillator approximations were used for ρ, with frequencies and rotational constants obtained at the MSX,[32] although anharmonic treatments[50,51,52,53] for ρ could be used as well. Sampling the crossing seam when evaluating P_{MN} via ensembles of trajectories (as in eqs 12 or 13) does include vibrational anharmonicity in P_{MN}.

The CP equations (eqs 10) are commonly used in semiclassical multistate trajectory theories,[40,41,54] such as the surface hopping,[55,56] mean field,[57] and decay-of-mixing[33,58] methods, where trajectories are typically propagated from reactants to products. Here, in contrast, the CP equations were propagated in short-time trajectories initiated near the crossing seam, which is likely appropriate for the localized nonadiabatic dynamics associated with some spin-forbidden systems, and we have incorporated this localized nonadiabatic dynamics into a statistical model. The present approach is similar to that of Hammes-Schiffer and Tully,[6] who used eq 10 in surface hopping trajectories initiated at the seam of avoided crossings for a model system. The present approach differs in three ways. First, we have neglected one kind of electronic/nuclear coupling by not allowing surface switches. This choice simplifies the calculation of the total spin-forbidden probability, requires fewer trajectories, and is likely a good approximation for weakly coupled systems. For more strongly coupled systems, it may be appropriate to employ statistical theories for P based on surface hopping (or decay of mixing) multistate trajectories, such as the approach in Ref. 6. Second, we have used a model for decoherence to localize the trajectories close to the crossing seam, whereas the method in Ref. 6 considered fully coherent electronic motion and required longer-lived trajectories. Third, we have used eq 10 to develop a statistical model (eqs 12–14).

The present statistical model incorporates a similar treatment of electronic decoherence as that of the CSDM multistate trajectory method.[33] In both methods, each nonadiabatic region is treated coherently, and decoherence (called de-mixing in the context of CSDM) is allowed only between these regions. The CSDM method was found to be the most accurate of several surface hopping, mean field, and decay of mixing multistate trajectory methods tested,[54,59] including methods with fully coherent electronic evolution, such as the fewest-switches surface hopping method,[55] and methods that allowed decoherence during the nonadiabatic event, such as the SCDM method.[58]

In summary, the present MNST method includes semiclassical models for dynamical, static, and nonlocal multidimensional effects as well as for electronic decoherence. For comparison, we also consider statistical calculations based on eq 1 and using both the "reference geometry" and "ensemble averaged" (P_X^{MSX} and $\langle P_X \rangle_{\mathbf{R}}$) implementations of the X = LZ, WC, and IWC methods. None of the one-dimensional models for P_X includes dynamical multidimensional effects. The ensemble-averaged models include static multidimensional effects, while the WC and IWC models include one-dimensional nonlocal interference effects.

II.C. Analytic diabatic potential energy surfaces

A three-state diabatic representation of the lowest-energy singlet (1 ^{1}A' or S0) and the two lowest-energy triplet (1 ^{3}A′ or T1 and 1 ^{3}A″ or T2) states of CO_2 was presented previously.[32] This representation included geometry-dependent spin-orbit coupling surfaces for the S0/T1 and S0/T2 interactions; the spin-orbit coupling between the T1 and T2 surfaces and other nonadiabatic couplings were neglected. The spin-forbidden dynamics at the S0/T1 and S0/T2 seams were therefore treated as independent of one other. The 3 triplet and 1 singlet spin states associated with each singlet/triplet crossing were reduced to a two state representation.[60]

The singlet and triplet potential energy surfaces were calculated using the dynamically weighted[61,62] MRCI+Q method extrapolated to the complete basis set limit. The spin-orbit coupling surfaces were calculated using the Breit-Pauli model[63] and the CASSCF/aug-cc-pVQZ method. Analytic representations of the diabatic potential energy and coupling surfaces were developed using the interpolated moving least squares (IMLS) semiautomated fitting method.[64,65] Molecular properties calculated using the fitted surfaces were previously shown to be in excellent agreement with available experimental information.

For both the T1 and T2 states of CO_2, conventional adiabatic saddle points precede the crossing seams. This was incorporated into the present statistical calculations via a straightforward generalization of universal statistical theory (UST).[66,67] The threshold energy for the spin-forbidden bottleneck (analogous to the saddle point energy in TST) was taken to be the zero-point inclusive energy of the MSX. While some spin-forbidden systems may feature significant anharmonic and/or nonstatistical effects, it was shown previously using semiclassical trajectories that these approximations do not introduce significant errors for this system.[32] The UST state counts were used to calculate thermal rate coefficients for each initial state (T1 and T2) using standard bimolecular reaction rate formulas.[12,14] The electronic partition function used here differs slightly from that of Ref. 32, as here we have considered lower temperatures; the spin-orbit split electronic states of ^3O were weighted by their thermal populations, whereas this splitting was neglected previously.

III. RESULTS

III.A. One-dimensional model systems

We first consider two model systems, each with one nuclear degree of freedom, r, and two electronic states. The models provide one-dimensional results to reference when quantifying multidimensional effects in the full-dimensional calculations reported in Sec. III.B. The molecular parameters for the model systems were based on the S0/T1 crossing seam for CO_2,[32] with a constant coupling surface of H_{SO} = 48 cm^{-1} and an asymptotic excitation energy of 45 kcal/mol. The range parameters for the exponential diabatic potential energy surfaces for Model 1 and the effective nuclear mass were chosen such that the mass-scaled slopes at the crossing point had magnitudes equal to those for the S0/T1 MSX for CO_2. For this model, the slopes of the two surfaces have the same sign at the crossing point. For Model 2, the range parameter for the excited electronic state was adjusted such that the slopes of the two electronic states have different signs but equal magnitudes at the crossing point.

Trajectories were initiated at large r for a range of collision energies, propagated toward an inner turning point at small r, and continued until the trajectory returned to large r. For Model 1, trajectories were initiated on either the ground state surface S or the excited state surface T. For Model 2, trajectories were initiated only on the ground state surface S, as the excited state surface is unbound. In the model surface calculations, each trajectory thus encountered the crossing point twice, once with $\dot{r} < 0$ and then with $\dot{r} > 0$.

The total CP nonadiabatic transition probability for both passages, P_{2CP}, was evaluated as a function of $E_\perp$, the kinetic energy at the crossing point, and is compared with P_{2LZ}, P_{WC}, and P_{IWC} in Fig. 2. For both model systems, P_{IWC} is in close agreement with P_{2CP}, while the P_{2LZ} model tends to the qualitatively incorrect low-energy adiabatic limit, as discussed by Delos[27] and mentioned above. The small differences in the 2CP and IWC predictions are likely due to the assumptions made about extrapolating the diabatic the potentials in the WC derivation, on which the IWC method is based. The 2CP and IWC methods both predict that the electronic dynamics can depend sensitively on the choice of the initially prepared electronic state, and these differences can be as large as a factor of 5 at low energies for Model 1 (cf. Fig. 2(a)). The WC result is intermediate of the electronic-state-dependent 2CP and IWC results. For more strongly coupled systems, the original WC model (eq 8) may be appropriate, but, at least in the present semiclassical context and for weakly coupled systems, the modification in eq 9 defining the IWC approach leads to state-dependent results that are in good agreement with those of the 2CP model at low energies. For Model 2, the slopes of the two surfaces at the crossing point have the same magnitudes but different signs, eqs 8 and 9 are therefore equivalent, and $P_{WC} = P_{IWC} \approx P_{2CP}$.

Although not shown in Fig. 2, the CP equations, like the IWC and WC methods, predict nonzero nonadiabatic transition probabilities for $E_\perp < 0$ that may be associated with tunneling. In the CP model, these tunneling events arise as the classical nuclear trajectory approaches the crossing seam close enough to transfer electronic population,

even if the trajectory does not have quite enough energy to access the seam. The probabilities predicted by the CP method for $E_\perp < 0$ are in good agreement with those of the IWC method.

At higher energies, the 2CP, WC, and IWC models oscillate rapidly about the 2LZ result, and all four methods are in good agreement with one another and are independent of the choice of initial electronic state, on average.

The comparisons in Fig. 2 demonstrate that the semiclassical CP method correctly predicts the weak coupling limit at energies near the crossing threshold, as well as interference effects arising from coherent double passages in one-dimensional systems. The high accuracy of the CP equations in one dimension has been reported often in the context of validating semiclassical trajectory theories, including validations using Tully's frequently revisited model systems.[55]

Next, we consider nonlocal phase interference effects in one dimension. The time spent between the incoming and outgoing seam encounters depends on the shape of the potential energy surface of the occupied electronic state. The electronic dynamics (and in particular the interference of the electronic phase) at the 2nd seam encounter depends sensitively on this time interval. This nonlocal effect is illustrated in Fig. 3, where, using Model 1, the electronic state populations of the initially unoccupied electronic states are shown as functions of the time along the trajectory. The electronic dynamics for both initial states and its dependence on energy are considered. For $E_\perp = 10$ (Fig. 3(a)) and for the T initial state, the time interval between crossings is $\Delta t = 14$ fs, while the timescale associated with each nonadiabatic event is shorter ($\tau_e \approx 5$ fs). The individual contributions to the overall electronic dynamics associated with each encounter with the seam (which for these one-dimensional models is a single geometry) may therefore be unambiguously assigned. The result of making a small change to $E_\perp$ (reducing it by 0.5 kcal/mol) for this case is also shown in Fig. 3(a). The electronic dynamics at the first seam counter are nearly identical for $E_\perp = 9.5$ and 10 kcal/mol. The time between seam encounters Δt is

slightly different at the two energies, however, such that at the second seam encounter the instantaneous value of the rapidly spinning electronic phase differs, and the electronic dynamics at the second encounter is significantly affected. Clearly, models that neglect electronic coherence between seam passages (such as the 2LZ method) may differ significantly from those that include this coherence (2CP, WC, and IWC), and this is reflected in the differences shown in Fig. 2 at low energies. At higher energies, the electronic phase is oscillating rapidly enough that these details wash out, and the CP and IWC results agree with the 2LZ result, on average.

For the three other cases shown in Fig. 3 ($E_\perp$ = 1 kcal/mol for both the S and T states $E_\perp$ = 10 kcal/mol for the S state), the time interval between surface crossings is short (Δt = 1–6 fs) and is similar to the timescale over which the semiclassical electronic transitions take place ($\tau_e \approx 5$ fs). When $\Delta t \leq \tau_e$, it is not readily apparent how one can assign contributions of the overall electronic dynamics to each surface crossing. Our strategy, as discussed in Sec. II, was to define the nonadiabatic interaction region for each seam encounter based on the next local minimum in the magnitude of the nonadiabatic coupling vector and then to average over the final ¼ of the interaction region. The horizontal lines in eq 2 are the results of these averages.

Decoherence is the loss of electronic phase information, which, in the present model, has the effect of localizing the nonadiabatic dynamics. Here, decoherence events are allowed between seam encounters but not during them. Fast decoherence in such a model does not completely eliminate the effects of nonlocal phase interference. As seen in Fig. 3, when $\Delta t \leq \tau_e$ the nonadiabatic dynamics at the *first* crossing is affected by the second one, even if our model would call for a decoherence event after the first seam crossing. This situation leads to two types of "single passage" low-$E_\perp$ transition probabilities in multidimensional systems, those with $\Delta t \leq \tau_e$, which feature nonlocal phase interference effects associated with the "weak coupling" limit, and those with $\Delta t >$

τ_e, which do not. The former can be seen in one-dimension, while the latter cannot. These two cases will be discussed in more detail below.

A comparison of first passage nonadiabatic transition probabilities is shown in Fig. 4 for the same one-dimensional systems considered in Fig. 2. The double passage probabilities for the WC and IWC models are shown divided by 2 and are labeled $P_{WC/2}$ and $P_{IWC/2}$. Qualitatively, the results for the first passage are similar to those observed for coherent double passages. Again at low energies, there is a significant difference in state-selected CP and IWC/2 transition probabilities, with differences as large as a factor of 3 for the two electronic states. Quantitatively, however, the CP method predicts lower nonadiabatic transition probabilities than those obtained by dividing the IWC result by 2. This may be explained by noting that the two passages do not generally contribute equally to the overall dynamics (cf. Fig. 3), and, on average, the first passage has smaller nonadiabatic transition probabilities than the second at low energies. Simply dividing the IWC results by two over-predicts the CP result by as much as a factor of 3. At high energies, the single passage CP, WC/2, and IWC/2 methods again agree with the LZ model, on average.

III.B. Multidimensional nonadiabatic transition probability

Next, we consider full-dimensional calculations of P_{CP} for CO_2 using the analytic diabatic surfaces and couplings summarized in Sec II.C. We initially restrict attention to the S0/T1 seam and to a single location on the crossing seam, the MSX. These calculations therefore do not include static multidimensional effects, but dynamical and nonlocal multidimensional effects are included. P_{CP} was calculated for ensembles of trajectories initiated at the S0/T1 MSX and on the T1 surface with the total energy E distributed microcanonically among the internal degrees of freedom. Full-dimensional trajectories were propagated "backwards" from the MSX until the beginning of the interaction region was identified. The resulting coordinates and momenta were then used

to initiate semiclassical trajectories as described in Sec. II. Each trajectory crossed the seam at the MSX such that the ensemble featured a microcanonical distribution of energy at the seam, including a distribution of $E_\perp$.

Multidimensional single-passage CP results for two total energies (E = 5 and 20 kcal/mol) are shown in Fig. 5, where each circle is the result of a single trajectory from the ensemble. These results are compared with the results of the $P_{\mathrm{LZ}}^{\mathrm{MSX}}$ and $P_{\mathrm{IWC/2}}^{\mathrm{MSX}}$ models and with the one-dimensional single-passage CP result for the S0/T1 MSX from Fig. 4. The multidimensional calculations, unlike the one-dimensional models, predict a range of electronic transition probabilities for each value of $E_\perp$. Furthermore, the spread of P_{CP} for a given $E_\perp$ is dependent on the total energy E, particularly at low $E_\perp$. This spread is as large as a factor of 2 for E = 5 kcal/mol (at $E_\perp$ = 1 kcal/mol) and broadens to as much as a factor of 20 for E = 20 kcal/mol at low $E_\perp$. Both the range of values of P_{CP} predicted for each $E_\perp$ and the dependence of this distribution on E arise due to dynamical multidimensional effects associated with differences in each trajectory's instantaneous total energy distribution as it encounters the seam. One-dimensional models are necessarily single valued in $E_\perp$ and independent of E.

Although not presented here in detail, the above analysis was repeated for ensembles prepared at other locations on the S0/T1 crossing seam and for several values of E. These results were qualitatively similar to those in Fig. 5, but some differences were found. Notably, for locations other than the MSX, the one-dimensional CP result was not necessarily a lower bound on the full-dimensional results at low $E_\perp$. The other ensembles also typically featured a wider range of multidimensional transition probabilities for given values of $E_\perp$ and E than those for the MSX ensemble. The fact that the MSX is a local minimum on the seam likely explains its somewhat atypical multidimensional dynamics.

The broad distribution of P_{CP} at low $E_\perp$ for moderate and high E is approximately bounded from above by the LZ result. This feature was found for all of the ensembles considered, including those prepared for geometries other than the MSX. This may be explained by identifying two qualitatively different classes of multidimensional low-$E_\perp$ trajectories: those that promptly return to the seam after crossing it and those that do not.

The first class features double-passage nonlocal interference effects similar to those identified in one-dimension; this effect arises even when computing P_{CP} for the first passage only, as discussed above. Phase interference between prompt double passages leads to the "weak coupling" limit at low $E_\perp$, and this class of trajectories is responsible for the values of P_{CP} clustered around the one-dimensional CP result shown in Fig. 5(d). Unlike in one dimension, however, the second seam crossing in multiple dimensions (however prompt) need not occur at the same location on the crossing seam as the first or with the same value of $E_\perp$. Small differences in local seam properties and in $E_\perp$ at nearby seam passages lead to multidimensional weak coupling values of P_{CP} that may differ from the one-dimensional result—by as much as a factor of 5 in Fig. 5(d). Again, for ensembles prepared for locations on the seam other than the MSX, and the range of P_{CP} associated with nonlocal multidimensional effects was found to be even greater than that for the MSX ensemble shown in Fig. 5(d).

The second class of trajectories has no analog in one dimension. An example of such a trajectory (for E = 20 and $E_\perp$ = 0.01 kcal/mol) is shown in Fig. 6. At the S0/T1 MSX, the crossing seam is approximately perpendicular to the OCO bond angle (θ_{OCO}). The trajectory shown in Fig. 6 was initiated at the small-θ_{OCO} side of the seam, experienced a turning point in one of the CO bond distances, and then crossed the seam at the MSX with a small value of $E_\perp$. After the seam crossing, the trajectory propagated in such a way that the next seam crossing was not encountered for 65 fs. (In contrast, the "prompt return" trajectories discussed above returned to the seam after only a few fs at low $E_\perp$ and would be difficult to discern if plotted as in Fig. 6.) The first seam crossing

was therefore isolated from the second one, and, despite the small value of $E_\perp$, no nonlocal interference effects occurred. The absence of interference leads to conditions that satisfy the *adiabatic* low-$E_\perp$ limit—not the weak coupling limit. This second class of multidimensional trajectories therefore gives values of P_{CP} that agree approximately with those of the LZ model, which also behaves adiabatically at low $E_\perp$. We note that both types of low-$E_\perp$ trajectories were found for seam crossings in either direction. Weak mode specificity was observed in low-$E_\perp$ trajectories' tendencies to tend to the adiabatic or weak coupling limits, but a detailed analysis of this mode specificity was not pursued.

Finally, we consider ensembles of trajectories appropriate for the evaluation of P_{MN} via eqs 12 and 13. In principle, the crossing seam could be sampled microcanonically. Instead, this distribution was approximated by initiating trajectories with coordinates and momenta sampled microcanonically from the nearby triplet well. Each trajectory was propagated until the crossing seam was encountered, and P_{CP} was evaluated as discussed above. The effect of this approximation to the seam's true microcanonical distribution on the resulting kinetics was likely small, as the MSX is close to the minimum of the triplet well (cf. Fig. 6). The present strategy greatly simplified the calculations. (Such an approach may be preferred in some applications, where nearby wells are assumed to be equilibrated but the seam is not.)

Distributions of first-passage multidimensional CP probabilities for the S0/T1 crossing seam and for two different total energies are shown in Fig. 7. These results may again be compared with the one-dimensional CP and P_{LZ}^{MSX} probabilities. The comparisons are qualitatively similar to those made in Fig. 5 for the MSX-only ensembles. In the full ensembles of Fig. 7, however, the seam could be crossed anywhere that was energetically accessible. The resulting static multidimensional effects (arising due to variations in H_{SO} and in the shape of the potential energy surfaces along the crossing seam) led to values of P_{CP} that varied more significantly than those in Fig. 5.

One can isolate the importance of static multidimensional effects by comparing $P_{\mathrm{LZ}}^{\mathrm{MSX}}$ and $\langle P_{\mathrm{LZ}} \rangle_{\mathbf{R}}$ for different values of E and $E_{\perp}$. While the values of $\langle P_{\mathrm{LZ}} \rangle_{\mathbf{R}} / P_{\mathrm{LZ}}^{\mathrm{MSX}}$ for a single seam crossing varied significantly, on average, $\langle P_{\mathrm{LZ}} \rangle_{\mathbf{R}} / P_{\mathrm{LZ}}^{\mathrm{MSX}} \approx 2$ for $E > 25$ kcal/mol and $E_{\perp} > 1$ kcal/mol and approached 4 for lower $E_{\perp}$. Static multidimensional effects were less important at low E, with $\langle P_{\mathrm{LZ}} \rangle_{\mathbf{R}} / P_{\mathrm{LZ}}^{\mathrm{MSX}} < 1.2$, on average, for the $E = 15$ kcal/mol results shown in Fig. 7(a). For this system, static multidimensional effects tended to increase the electronic transition probability due to the increase of H_{SO} away from the MSX.[32]

P_{MN} was evaluated via eq 12, binning and averaging the results with respect to $E_{\perp}$, and interpolating in both $E_{\perp}$ and E. This representation of P_{MN} is shown in Fig. 7, along with a representation of the $\langle P_{\mathrm{LZ}} \rangle_{\mathbf{R}}$ method obtained in a similar way and for the same ensembles. At moderate and high $E_{\perp}$, the P_{MN} and $\langle P_{\mathrm{LZ}} \rangle_{\mathbf{R}}$ methods agree with each other, suggesting that while static multidimensional effects can be significant (increasing the nonadiabatic transition probability by as much as a factor of 2 at high E) dynamical and nonlocal multidimensional effects are likely negligible. At lower $E_{\perp}$, however, all three multidimensional effects can be important. By comparing P_{MN} and $\langle P_{\mathrm{LZ}} \rangle_{\mathbf{R}}$ at low $E_{\perp}$, we may quantify that dynamical and nonlocal multidimensional effects together act to lower the electronic transition probability by as much as a factor of 4. Overall, then, there is some cancellation of the effects of static, dynamical, and nonlocal multidimensional effects at low $E_{\perp}$, such that P_{MN} (which includes all three multidimensional effects) is in fair agreement with $P_{\mathrm{LZ}}^{\mathrm{MSX}}$ (which includes none). In fact, including just a single multidimensional effect can be less accurate than neglecting all of them, e.g., including only static multidimensional effects at low $E_{\perp}$.

The lowering of the nonadiabatic transition probability at low $E_{\perp}$ relative to the LZ model arises in part due to the presence of "prompt return" trajectories, as discussed

above. This class of low-$E_\perp$ trajectories was associated with the one-dimensional weak coupling limit, while another class of trajectories was associated with the adiabatic limit. Notably, in the full ensembles of Fig. 7, "adiabatic limit" trajectories are shown to significantly outnumber "weak coupling limit" ones. Despite the clear preference for the WC model over the LZ model in one dimension, the present results indicate that the WC limit is not necessarily an improvement over the LZ model in polyatomic applications.

Ensembles were prepared as described above for ten values of E up to 75 kcal/mol and for both the S0/T1 and S0/T2 crossing seams. P_{MN} was calculated for each ensemble via eq 12. For this system, the decoherence timescales τ_{d} evaluated at each seam crossing were always shorter than the time between seam encounters, and eq 12 reduced quantitatively to eq 13. While τ_{d} is generally expected to be short, the general accuracy of eq 13 as an approximation to eq 12 is unclear.

In practice, it was found convenient to calculate $P_{\mathrm{CP}}/P_{\mathrm{LZ}}^{\mathrm{MSX}}$ for each trajectory, and then to bin and average this ratio with respect to $E_\perp$ for each ensemble. This correction to $P_{\mathrm{LZ}}^{\mathrm{MSX}}$ was then interpolated in E and $E_\perp$ and applied to $P_{\mathrm{LZ}}^{\mathrm{MSX}}$ when evaluating eq 14. P_{MN} was assumed to be independent of the total angular momentum J.

III.C. Spin-forbidden kinetics

As summarized in Sec. II, the MNST spin-forbidden state count N^* from eq 14 was used along with the TST flux for the adiabatic transition state for the preceding saddle point in a two-transition state model. The adiabatic saddle points were found to be significantly rate limiting only at low temperature for the T1 state. Thermal (high-pressure-limit capture) rate coefficients k_∞ were obtained from the two-transition-state MNST state counts for each of the two reactive triplet states (T1 and T2). The total high pressure limit rate coefficient for ^{3}O + CO is the sum of the rate coefficients for the T1 and T2 surfaces.

MNST rate coefficients for each initial state and their total are shown in Fig. 8. Also shown are previously calculated CSDM rate coefficients,[32] which are 15-50% and ~2x larger than the MNST results for the T1 and T2 states, respectively. This discrepancy can be attributed largely to differences in the threshold energies for the crossing seams in the two calculations. Quantal thresholds were used in the MNST calculations, whereas the trajectory results necessarily reflect classical thresholds. The MNST calculations were repeated using classical threshold energies for the MSXs (i.e., with zero-point corrections to the MSXs neglected), and the results are in good agreement with the CSDM rate coefficients, as shown in Fig. 8. The good agreement between the classical MNST and CSDM results confirms that errors associated anharmonicity and nonstatistical effects in the MNST calculations are likely small for this system.

The MNST rate coefficients were fit to the following modified Arrhenius expressions for T = 300–5000 K

$$k_\infty^{\mathrm{T1}}(T) = 4.38\times10^{-12}(T/300\,\mathrm{K})^{-0.565}\exp(-3620\,\mathrm{K}/T) \quad \mathrm{cm^3\ molecule^{-1}\ s^{-1}}$$

$$k_\infty^{\mathrm{T2}}(T) = 1.50\times10^{-13}(T/300\,\mathrm{K})^{-0.385}\exp(-3834\,\mathrm{K}/T) \quad \mathrm{cm^3\ molecule^{-1}\ s^{-1}}$$

$$k_\infty(T) = 3.04\times10^{-12}(T/300\,\mathrm{K})^{-0.308}\exp(-3494\,\mathrm{K}/T) \quad \mathrm{cm^3\ molecule^{-1}\ s^{-1}}.$$

These are expected to be more accurate than those previously given based the CSDM results[32] due to the present use of quantal thresholds. A detailed error analysis was given in Ref. 32, and the CSDM results were assigned an error of 40%, principally arising from uncertainties in the accuracy of the calculated spin–orbit coupling strength. Unfortunately, the error associated with the use of classical thresholds was not considered in the previous analysis. The present rate expressions may be assigned an uncertainty of 40%, again principally due to the calculation of the spin–orbit coupling strength.

Also shown in Fig. 8 is the rate coefficient for the T1 initial state calculated using eq 1 and $P = P_{\mathrm{LZ}}^{\mathrm{MSX}}$. As in the MNST calculations, the UST model, RRHO approximation, and quantal thresholds were used. This method has been called “NA TST” elsewhere, and it is much simpler to evaluate than the present MNST model. As this approach does not

rely on identifying the minimum in the nuclear flux along the reaction coordinate as the dynamical bottleneck for the reaction, we refrain from labeling it a transition state theory and instead label it LZ/MSX. The LZ/MSX results differ from the MNST results by only 15% at 300 K and by ~50% at 5000 K. Based on the preceding analysis of the results in Fig. 7, the principal source of error in the LZ/MSX calculation may be identified as its neglect of static multidimensional effects; its good accuracy for this system likely benefits from some cancellation of errors, as well.

The MNST method is readily applied at low temperatures, whereas the previously reported CSDM calculations[32] were prohibitively expensive below ~1000 K due to the infrequence of spin-forbidden transitions at low temperatures. The MNST method predicts significant temperature dependence in k_∞ below 1000 K. For example, k_∞(300 K) is only 2.7 x 10^{-17} cm^3 $molecule^{-1}$ s^{-1}, 17000x slower than k_∞(3000 K). The low temperature (300–1000 K) MNST results are within a factor of ~5 of the high-pressure limit rate coefficient given by Troe[30] that is used in many combustion models.

IV. Summary and Conclusions

A multidimensional nonadiabatic statistical theory (MNST) for calculating spin-forbidden reaction rates was described and applied to the ^3O + CO reaction. The MNST method was shown to accurately predict rate coefficients previously obtained using CSDM multistate trajectories, so long as consistent thresholds are used. We note that the CSDM method was previously shown[54] to be the most accurate of several surface hopping, mean field, and decay of mixing semiclassical trajectory methods tested, with an average error of only ~20% relative to quantum scattering results averaged over a variety of nonadiabatic coupling types. The present validation of the MNST approach thus provides a statistical approach of similar accuracy to complement the CSDM method and other multistate trajectory approaches for characterizing spin-forbidden reactions.

The MNST method, like all statistical approaches, has several advantages over trajectory-based methods. First, quantum mechanical thresholds and state count formulas

may be readily used in statistical calculations, whereas "zero point violations" and related problems can lead to significant errors in trajectory calculations. The use of classical threshold energies, for example, was shown here to be a significant source of error in the previous CSDM calculations. Second, the development of high-level global descriptions of multiple potential energy surfaces and their couplings suitable for trajectory calculations is not straightforward for polyatomic systems. Statistical theories such as MNST require a less global characterization the potential energy surfaces and couplings. Likewise, direct dynamics applications of the MNST method are facilitated by its reliance on only short-time (~20 fs) trajectories. Third, statistical theories can be readily used to calculate low-probability events, whereas trajectory-based methods may require a prohibitive number of trajectories to do so. The room-temperature rate coefficients obtained here via MNST would have required millions of CSDM trajectories, for example. Fourth, pressure dependence in reaction rate coefficients can be characterized accurately[68] via master equation[69] calculations, which require statistical representations of the reactive flux. Similarly, rate coefficients for complex systems involving multiple intermediate wells and competitive branching to multiple products are often calculated using the master equation and statistical theories.

The MNST method shares the deficiencies of statistical theories, as well. Like all statistical theories, MNST cannot be used obtain internal energy distributions and may suffer from errors due to non-RRKM effects. MNST calculations share the same sources of error that arise in applications of TST, including those due to errors in the computed threshold energy and due to the typical neglect of vibrational anharmonicity. Here we focused on quantifying errors unique to spin-forbidden statistical calculations, namely those that are associated with the formulation of the nonadiabatic transition probability P. The MNST model for P was tested against several spin-forbidden statistical theories that use one-dimensional models for P, including the Landau-Zener, weak coupling, and improved weak coupling models. These comparisons were used to quantify errors

associated with the neglect of multidimensional effects that are not typically included in spin-forbidden statistical calculations

Namely, we identified three categories of multidimensional effects: static, dynamical, and nonlocal. Static multidimensional effects were shown to be the most significant for this system; their neglect led to errors as large as a factor of 2 in the thermal rate coefficient. Dynamical and nonlocal multidimensional effects were less important, but were non-negligible under some conditions (particularly for transitions with small values of $E_\perp$, the energy along the spin-forbidden reaction coordinate). We note that the crossing seam for CO_2 is only two-dimensional. The importance of multidimensional effects in larger systems with higher-dimensional crossing seams is unknown.

The role of electronic decoherence in localizing nonadiabatic dynamics near the crossing seam was analyzed. For this system, the rate of electronic decoherence was found to be much faster than the time between seam crossings, such that the present calculation required the consideration of only "single passage" trajectories. This localization greatly simplified and reduced the cost of the MNST calculations.

Finally, the present analysis showed that the "weak coupling" low-$E_\perp$ limit of the one-dimensional nonadiabatic transition probability is not always appropriate for polyatomic systems. Instead, some multidimensional systems access the crossing seam with small values of $E_\perp$ without promptly returning to the seam. This situation leads to nonadiabatic transition probabilities that tend to the adiabatic limit, and not the weak coupling limit, at low $E_\perp$. For CO_2, the majority of low-$E_\perp$ trajectories behaved adiabatically.

Acknowledgments

This work is supported by the Division of Chemical Sciences, Geosciences, and Biosciences, Office of Basic Energy Sciences, U.S. Department of Energy. Sandia is a

multiprogram laboratory operated by Sandia Corporation, a Lockheed Martin Company, for the United States Department of Energy under Contract No. DE-AC04-94-AL85000. Software development was supported by the AITSTME project as part of the Predictive Theory and Modeling component of the Materials Genome Initiative.

Figure Captions

Fig. 1. Representative reaction probabilities evaluated at the critical surface and shown as functions of the energy in the reaction coordinate for classical transition state theory, for semiclassical tunneling, and for weak coupling nonadiabatic transitions.

Fig. 2. Coherent double passage nonadiabatic transition probabilities for two one-dimensional model systems. Results for the 2LZ (red dashed lines), 2CP (black solid lines), WC (blue dashed lines) and IWC (blue solid lines) are shown. High-energy oscillations for some curves occur more rapidly than the resolution of the data used to make the plot. Some of the rapidly oscillating curves were truncated at high energy to better show the other curves. For model 1 (a), dependence on the T or S initial state is indicated by the thickness of the lines, with the 2LZ and WC results independent of this choice. For Model 2 (b), $P_{\mathrm{WC}} = P_{\mathrm{IWC}}$.

Fig. 3. CP nonadiabatic population transferred along trajectories initiated in the ground state S (thick solid black line) or excited state T (dotted black line) for the one-dimensional Model 1 system and for two total energies: $E_{\perp}$ = (a) 10 and (b) 1 kcal/mol. The straight lines indicate the times of the seam crossings and the values of P_{CP} calculated as discussed in the text. An excited state T trajectory for $E_{\perp}$ = 9.5 kcal/mol is shown as a thin dashed blue line in (a).

Fig. 4. Single-passage nonadiabatic transition probabilities for two one-dimensional model systems. Plotting conventions are as in Fig. 2.

Fig. 5. Single-passage multidimensional CP transition probabilities (black circles) for ensembles of 2500 trajectories crossing the S0/T1 seam at the MSX for two total energies: (a) 5 and (b) 20 kcal/mol. (b) and (d) are dual log plots of same information as (a) and (c), respectively. Also shown are the results of three one-dimensional models: $P_{\mathrm{LZ}}^{\mathrm{MSX}}$ (dashed red line), $P_{\mathrm{IWC/2}}^{\mathrm{MSX}}$ (dashed blue line), and the one-dimensional CP result (solid green line).

Fig. 6. Contour plot of the T1 surface of CO_2 shown as a function of the incipient bond distance R_{CO} and the OCO bond angle θ_{OCO}. An energy of zero relative to the asymptotic ^3O + CO energy is shown as a thick solid black line. Thin solid black lines indicate contour increments of 10 kcal/mol. Contours indicating 1, 2, …, 9 kcal/mol are shown as dashed lines. The adiabatic saddle point and minimum on the crossing seam (MSX) are indicated by o and x, respectively. The crossing seam is shown as a thick red line. A seam-crossing trajectory is shown as a dashed blue line, where the thick segment of the line indicates the beginning of the trajectory.

Fig. 7. Single-passage multidimensional CP transition probabilities (black circles) for ensembles of 1500 trajectories crossing the S0/T1 seam and for two total energies: (a) 15 and (b) 75 kcal/mol. Also shown are the results of two one-dimensional models: P_{LZ}^{MSX} (dashed red lines) and the one-dimensional CP result (solid green line). The representation of P_{MN} obtained by averaging and binning the CP results is shown (dashed blue lines), along with a similar representation of the $\langle P_{LZ} \rangle_{\mathbf{R}}$ results (dash-dotted orange line).

Fig. 8. High-pressure-limit rate coefficient for the ^3O + CO reaction calculated via MNST (solid lines) for the T1 (red) and T2 (blue) initial states and their total (black). These results are compared with MNST rate coefficients obtained using classical thresholds (thick dashed lines) and with the CSDM multistate trajectory results of Ref. 32 (symbols). Also shown is the rate coefficient predicted by the LZ/MSX model for the T1 initial state (thin red dash-dotted line).

Figure 1

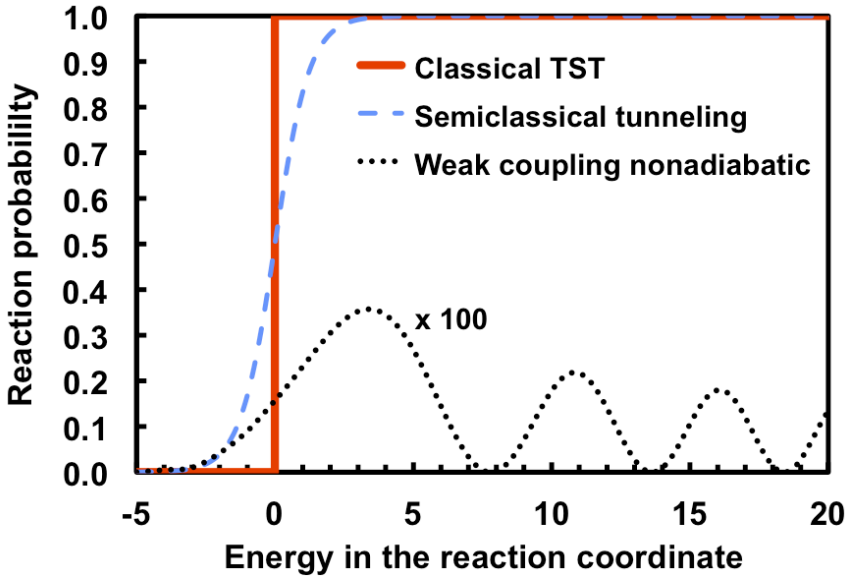

Fig. 1. Representative reaction probabilities evaluated at the critical surface and shown as functions of the energy in the reaction coordinate for classical transition state theory, for semiclassical tunneling, and for weak coupling nonadiabatic transitions.

Figure 2

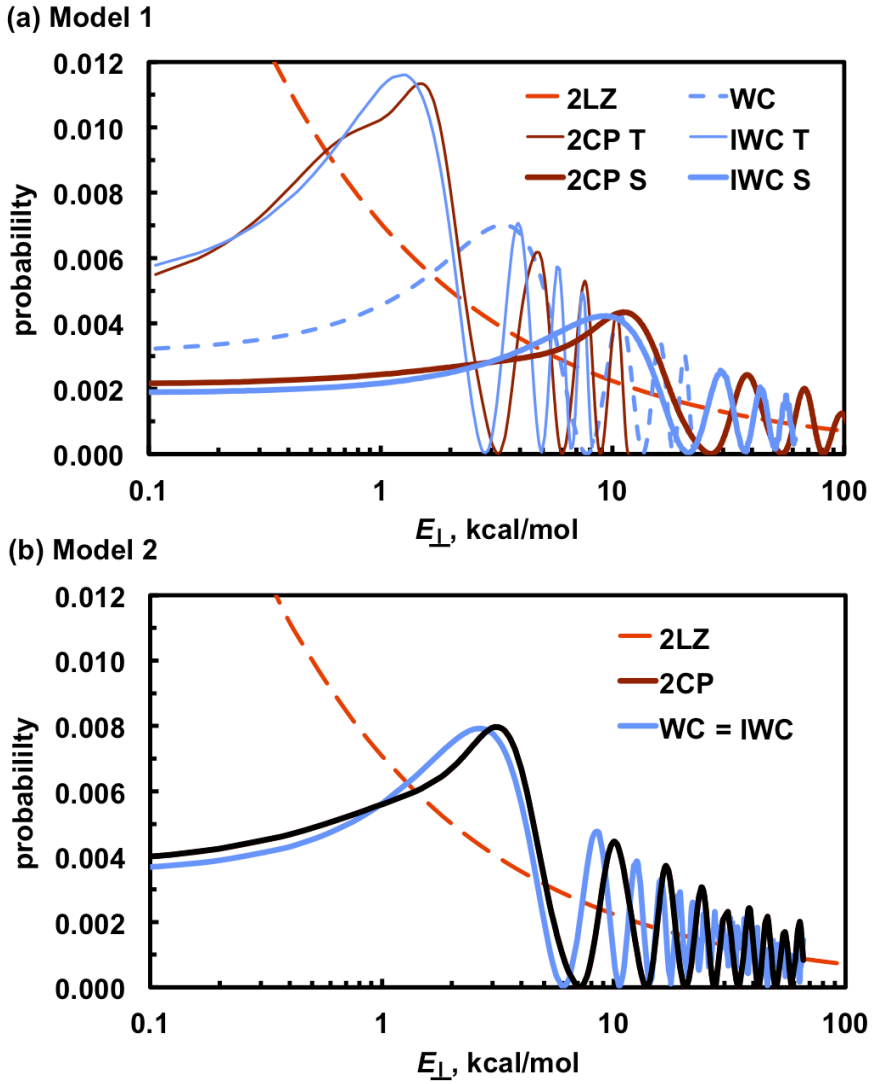

Fig. 2. Coherent double passage nonadiabatic transition probabilities for two one-dimensional model systems. Results for the 2LZ (red dashed lines), 2CP (black solid lines), WC (blue dashed lines) and IWC (blue solid lines) are shown. High-energy oscillations for some curves occur more rapidly than the resolution of the data used to make the plot. Some of the rapidly oscillating curves were truncated at high energy to better show the other curves. For model 1 (a), dependence on the T or S initial state is indicated by the thickness of the lines, with the 2LZ and WC results independent of this choice. For Model 2 (b), $P_{WC} = P_{IWC}$.

Figure 3

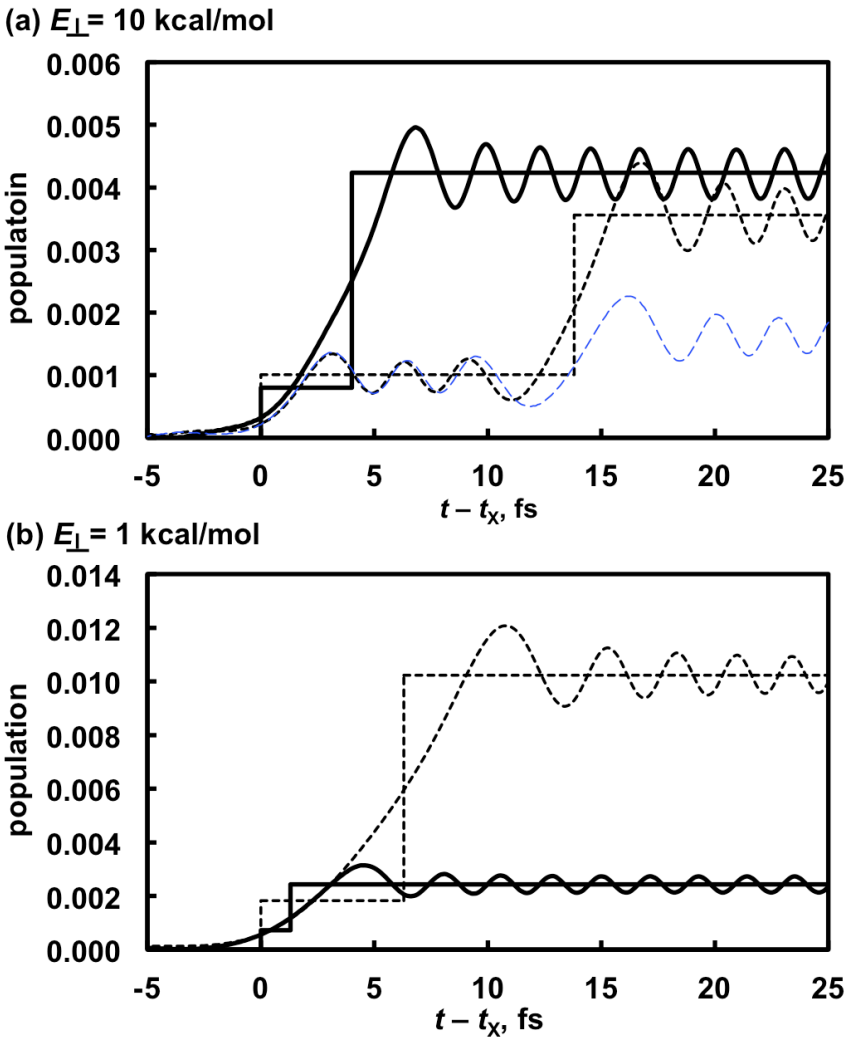

Fig. 3. CP nonadiabatic population transferred along trajectories initiated in the ground state S (thick solid black line) or excited state T (dotted black line) for the one-dimensional Model 1 system and for two total energies: $E_\perp$ = (a) 10 and (b) 1 kcal/mol. The straight lines indicate the times of the seam crossings and the values of P_{CP} calculated as discussed in the text. An excited state T trajectory for $E_\perp$ = 9.5 kcal/mol is shown as a thin dashed blue line in (a).

Figure 4

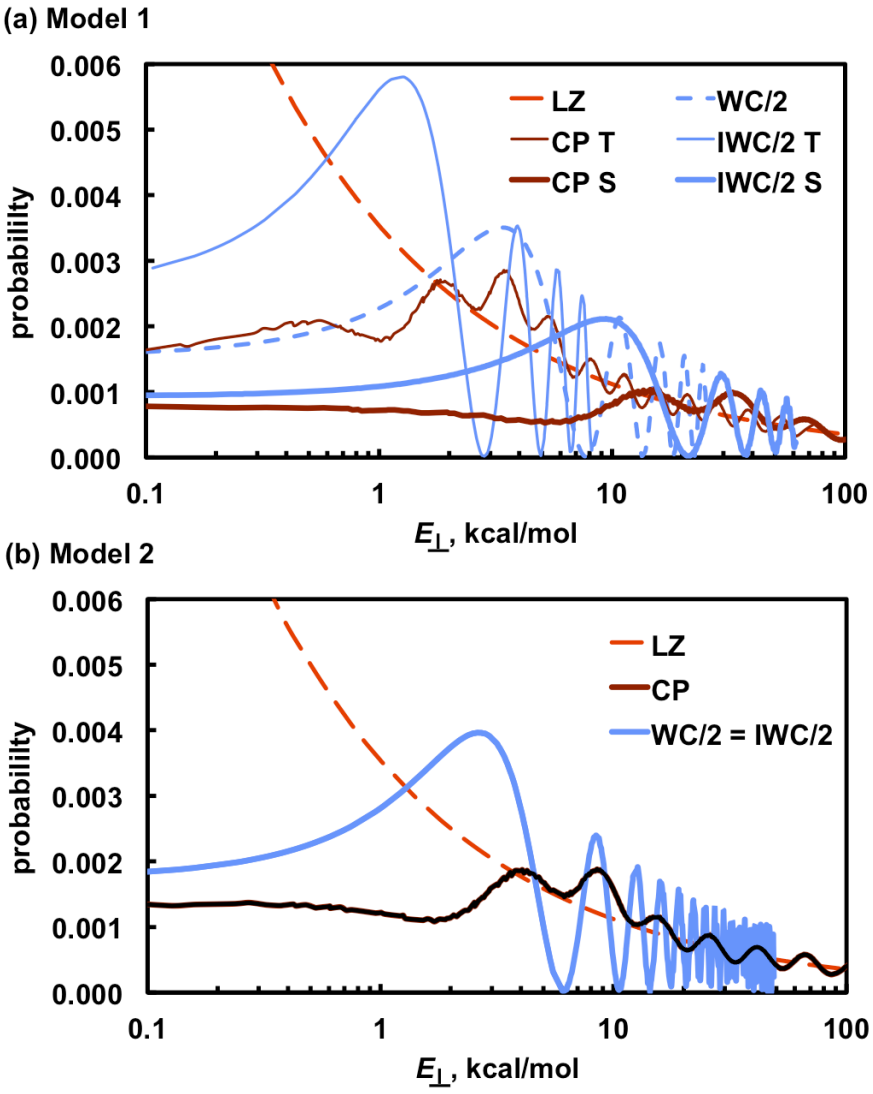

Fig. 4. Single-passage nonadiabatic transition probabilities for two one-dimensional model systems. Plotting conventions are as in Fig. 2.

Figure 5

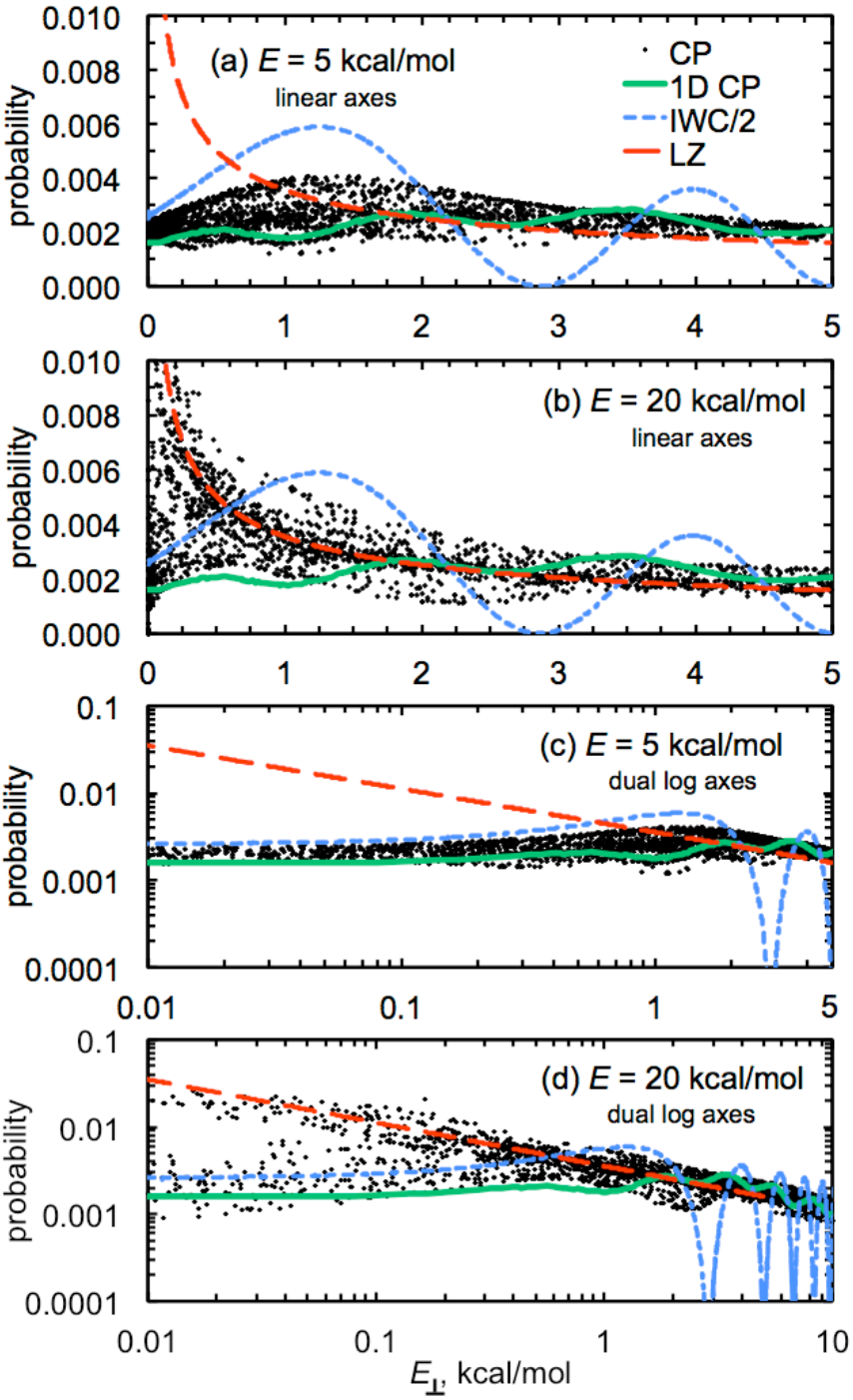

Fig. 5. Single-passage multidimensional CP transition probabilities (black circles) for ensembles of 2500 trajectories crossing the S0/T1 seam at the MSX for two total energies: (a) 5 and (b) 20 kcal/mol. (b) and (d) are dual log plots of same information as (a) and (c), respectively. Also shown are the results of three one-dimensional models: $P_{\mathrm{LZ}}^{\mathrm{MSX}}$ (dashed red line), $P_{\mathrm{IWC/2}}^{\mathrm{MSX}}$ (dashed blue line), and the one-dimensional CP result (solid green line).

Figure 6

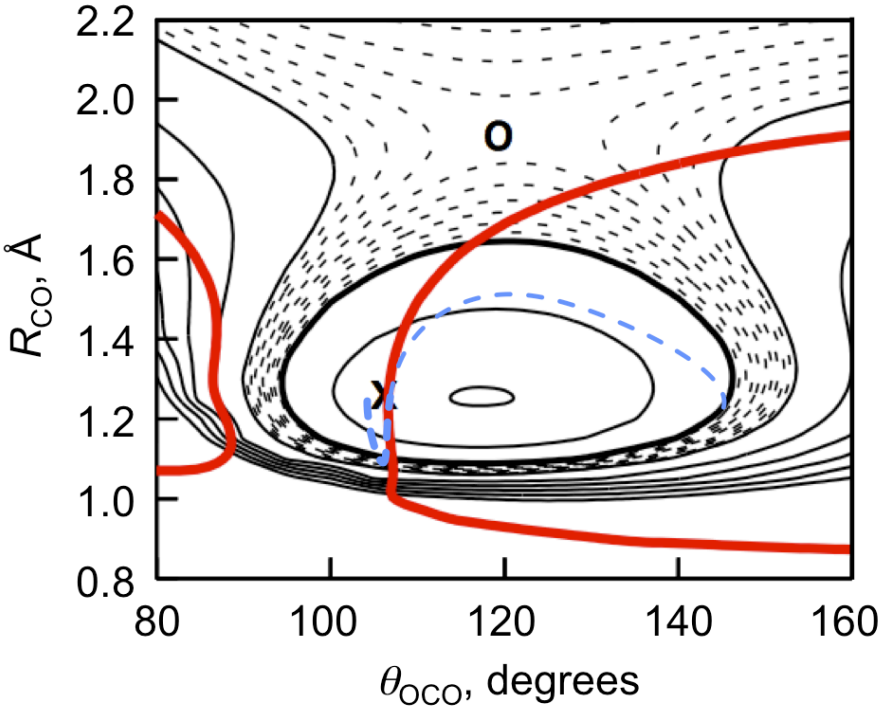

Fig. 6. Contour plot of the T1 surface of CO_2 shown as a function of the incipient bond distance R_{CO} and the OCO bond angle θ_{OCO}. An energy of zero relative to the asymptotic ^3O + CO energy is shown as a thick solid black line. Thin solid black lines indicate contour increments of 10 kcal/mol. Contours indicating 1, 2, …, 9 kcal/mol are shown as dashed lines. The adiabatic saddle point and minimum on the crossing seam (MSX) are indicated by o and x, respectively. The crossing seam is shown as a thick red line. A seam-crossing trajectory is shown as a dashed blue line, where the thick segment of the line indicates the beginning of the trajectory.

Figure 7

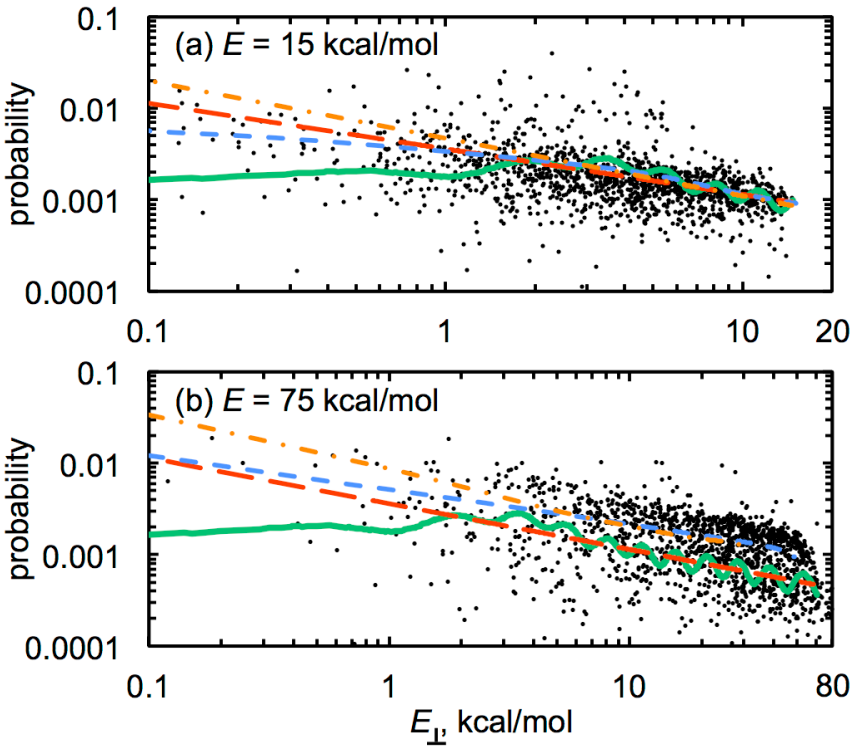

Fig. 7. Single-passage multidimensional CP transition probabilities (black circles) for ensembles of 1500 trajectories crossing the S0/T1 seam and for two total energies: (a) 15 and (b) 75 kcal/mol. Also shown are the results of two one-dimensional models: P_{LZ}^{MSX} (dashed red lines) and the one-dimensional CP result (solid green line). The representation of P_{MN} obtained by averaging and binning the CP results is shown (dashed blue lines), along with a similar representation of the $\langle P_{LZ} \rangle_{\mathbf{R}}$ results (dash-dotted orange line).

Figure 8

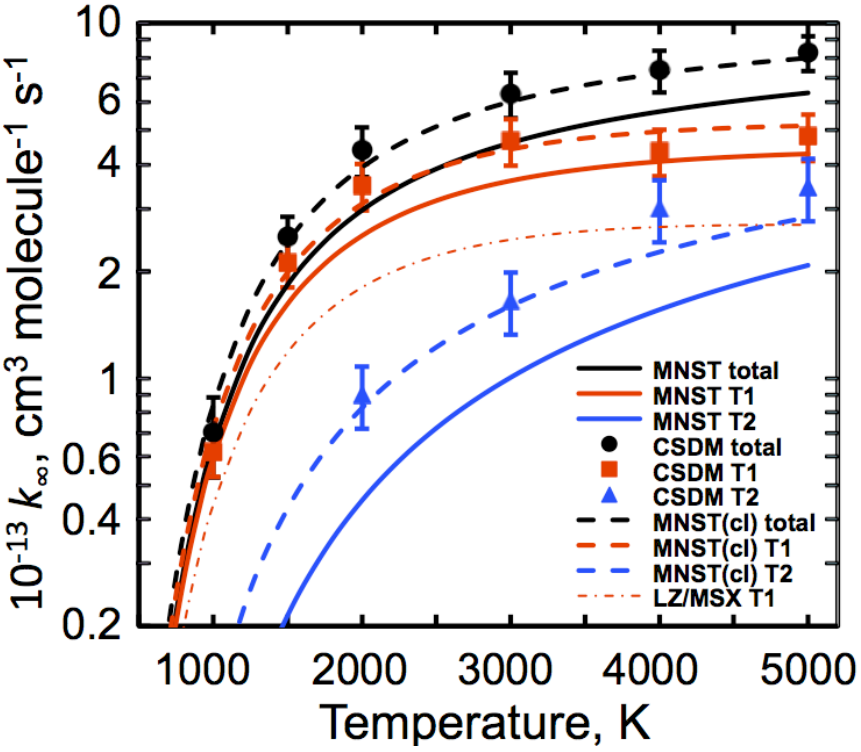

Fig. 8. High-pressure-limit rate coefficient for the ^{3}O + CO reaction calculated via MNST (solid lines) for the T1 (red) and T2 (blue) initial states and their total (black). These results are compared with MNST rate coefficients obtained using classical thresholds (thick dashed lines) and with the CSDM multistate trajectory results of Ref. 32 (symbols). Also shown is the rate coefficient predicted by the LZ/MSX model for the T1 initial state (thin red dash-dotted line).

References

[1] Tully, J. C. Collision complex model for spin-forbidden reactions: Quenching of O by N_2. *J. Chem. Phys.* **1974**, *61*, 61–68.

[2] Zahr, G. E.; Preston, R. K.; Miller, W. H. Theoretical treatment of quenching in O + N_2 collisions. *J. Chem. Phys.* **1975**, *62*, 1127–1135.

[3] Lorquet, J. C.; Leyh-Nihant B. Nonadiabatic unimolecular reactions. 1. A statistical formulation for the rate constants. *J. Phys. Chem.* **1988**, *92*, 4778–4783.

[4] Marks A. J.; Thompson D. L. A phase-space theory and Monte Carlo sampling method for studying nonadiabatic unimolecular reactions. *J. Chem. Phys.*, **1992**, *96*, 1911–1918.

[5] Sahm, D. K.; Thompson, D. L. Comparison of trajectory surface hopping and Monte Carlo phase-space theory predissociation rate contants for N_2O. *Chem. Phys. Lett.* **1993**, *210*, 175–179.

[6] Hammes-Schiffer, S.; Tully, J. Nonadiabatic transition state theory and multiple potential energy surface molecular dynamics of infrequent events. *J. Chem. Phys.* **1995**, *103*, 8528–8537.

[7] Topaler, M. S.; Truhlar, D. G. Statistical model for nonadiabatic decay of an exciplex strongly coupled to a dissociative continuum. *J. Chem. Phys.* **1997**, *107*, 392–401.

[8] Harvey, J. N.; Aschi, M. Spin-forbidden dehydrogenation of methoxy cation: a statistical view. *Phys. Chem. Chem. Phys.* **1999**, *1*, 5555–5563.

[9] Cui, Q.; Morokuma, K.; Bowman, J. M.; Klippenstein, S. J. The spin-forbidden reaction $CH(^2P) + N_2 \rightarrow HCN + N(^4S)$ revisited. II. Nonadiabatic transition state theory and application. *J. Chem. Phys.* **1999**, 110, 9469–9482.

[10] Marks, A. J. Nonadiabatic transition-state theory: A Monte Carlo study of competing bond fission process in bromoacetyl chloride. *J. Chem. Phys.* **2001**, *114*, 1700–1708.

[11] Zhao, Y.; Mil'nikov, G.; Nakamura, H. Evaluation of canonical and microcanonical nonadiabatic rate constants by using the Zhu–Nakamura formulas. *J. Chem. Phys.* **2004**, *121*, 8854–8860.

[12] Harvey, J. N. Understanding the kinetics of spin-forbidden chemical reactions. *Phys. Chem. Chem. Phys.* **2007**, *9*, 331–343.

[13] Wigner, E. The transition state method. *Trans. Faraday Soc.*, **1938**, *34*, 29–41.

[14] Fernandez-Ramos, A.; Miller, J. A.; Klippenstein, S. J.; Truhlar, D. G. Modeling the kinetics of bimolecular reactions. *Chem. Rev.* **2006**, *106*, 4518–4584.

[15] By which we mean his 3rd assumption. His first two assumptions are (1) the Born–Oppenheimer separation of the nuclear and electronic variables, and (2) the classical treatment of the nuclear variables.

[16] Miller, W. H. Importance of nonseparability in quantum mechanical transition-state theory. *Acc. Chem. Res.* **1976**, *9*, 306–312.

[17] Pechukas, P.; Pollak, E. *J. Chem. Phys.* Classical transition state theory is exact if the transition state is unique. **1979**, *71*, 2062–2068.

[18] Fernandez-Ramos, A., Miller, J. A., Klippenstein, S. J., and Truhlar, D. G. Modeling the kinetics of bimolecular reactions. *Chem. Rev.* **2006**, *106*, 4518–4584.

[19] Miller, W. H. Quantum mechanical transition state theory and a new semiclassical model for reaction rate constants. *J. Chem. Phys.* **1974**, *61*, 1823–1834.

[20] Marcus, R. A.; Coltrin, M. E. A new tunneling path for reactions such as $H + H_2 \rightarrow H_2 + H$. *J. Chem. Phys.* **1977**, *67*, 2609–2613.

[21] Skodje, R. T.; Truhlar, D. G.; Garrett, B. C. A general small-curvature approximation for transition-state-theory transmission coefficients. *J. Phys. Chem. A* **1981**, *85*, 3019–3023.

[22] Miller, W. H.; Hernandez, R.; Handy, N. C.; Jayatilaka, D.; Willets, A. Ab initio calculation of anharmonic constants for a transition state, with application to

semiclassical transition state tunneling probabilities. *Chem. Phys. Lett.* **1990**, 172, 62–68.

[23] Lynch, G. C.; Truhlar, D. G.; Garrett, B. C. Test of the accuracy of small-curvature and minimum-energy reference paths for parametrizing the search for least-action tunneling paths. *J. Chem. Phys.* **1989**, *90*, 3102–3109.

[24] Wagner, A. F. Improved multidimensional semiclassical tunneling theory. *J. Phys. Chem. A* 2013, 177, 13089–13100.

[25] Truhlar, D. G. "Decoherence in Combined Quantum Mechanical and Classical Mechanical Methods for Dynamics as Illustrated for Non-Born–Oppenheimer Trajectories," in *Quantum Dynamics of Complex Molecular Simulations*, edited by D. A. Micha and I. Burghardt (Springer, Berlin, 2007), pp. 227–243.

[26] Nikitin, E. E. Non-adiabatic transitions near the turning point in atomic collisions. *Opt. Spectrosk.* **1961**, *11*, 452–456.

[27] Delos, J. B. On the reactions of N_2 with O. *J. Chem. Phys.* **1973**, *59*, 2365.

[28] Coveney, P. V.; Child, M. S.; Barany, A. The two-state S matrix for the Landau–Zener potential curve crossing model: Predissociation and resonant scattering. *J. Phys. B: At. Mol. Phys.* **1985**, *18*, 4557–4580.

[29] Allen, M. T.; Yetter, R. A.; Dryer, F. L. High pressure studies of moist carbon monoxide/nitrous oxide kinetics. *Combust. Flame* **109**, 449 (1997).

[30] Troe, J. Thermal dissociation and recombination of polyatomic molecules. *Fifteenth Symp. (Int.) Combust.* **1975**, *15*, 667–680.

[31] Hwang, D.-Y.; Mebel, A. M. Ab initio study of spin-forbidden unimolecular decomposition of carbon dioxide. *Chem. Phys.* **2000**, *256*, 169–176.

[32] Jasper, A. W.; Dawes, R. Non-Born–Oppenheimer molecular dynamics of the spin-forbidden reaction O + CO → CO_2. *J. Chem. Phys.* **2013**, *139*, 154313.

[33] Zhu, C.; Nangia, S.; Jasper, A. W.; Truhlar, D. G. Coherent switching with decay of mixing: An improved treatment of electronic coherence for non-Born–Oppenheimer trajectories. *J. Chem. Phys.* **2004**, *121*, 7658–7670.

[34] Noga, K.; Morokuma, K. Determination of the lowest-energy point on the crossing seam between two potential surfaces using the energy gradient. *Chem. Phys. Lett.* **1985**, *119*, 371–374.

[35] Harvery, J. N.; Aschi, M.; Schwarz, H.; Koch, W. The singlet and triplet states of the phenyl cation. A hybrid approach for locating minimum energy crossing points between non-interacting potential energy surfaces. *Theor. Chem. Acc.* **1998**, *99*, 95–99.

[36] Landau, L. D. *Phys. Z.* **1932**, *2*, 46. Zener, C. Proc. R. Soc. London A **1932**, *137*, 696.

[37] Wittig, C. The Landau–Zener formula. *J. Phys. Chem. B* **2005**, *109*, 8429–8430.

[38] Jones, G. A.; Paddon-Row, M. N.; Carpenter, B. K.; Piotrowiak, P. Symmetry-forbidden vs symmetry-allowed electron and hole transfer in medium sized intramolecular organic donor-accceptor radical ions. A trajectory surface hopping study. *J. Phys. Chem. A* **2002**, *106*, 5011–5021.

[39] Park, K.; Engelkemier, J.; Persico, M.; Manikandan, P.; Hase, W. L. Algorithms for sampling a quantum microcanoncial ensemble of harmonic oscillators at potential minima and conical intersections. *J. Phys. Chem. A* **2011**, *115*, 6603–6609.

[40] Tully, J. C. in "Modern Methods for Multidimensional Dynamics and Computations in Chemistry," edited by Thompson, D. L. (World Scientific, Singapore, 1998), pp. 34–72.

[41] Jasper, A. W.; Truhlar, D. G. Non-Born–Oppenheimer molecular dynamics for conical intersections, avoided crossings, and weak interactions. *Adv. Ser. Phys. Chem.* **2011**, *17*, 375–412.

[42] Parlant, G.; Gislason, E. A. An exact trajectory surface hopping procedure: Comparision with exact quantal calculations. *J. Chem. Phys.* **1989**, *91*, 4416–4418.

[43] Turi, L.; Rossky, P. J. Critical evaluation of approximate quantum decoherence rates for an electronic transition in methanol solution. *J. Chem. Phys.* **2004**, *120*, 3688.

[44] Jasper, A. W.; Truhlar, D. G. Non-Born–Oppenhiemer molecular dynamics of Na···FH. *J. Chem. Phys.* **2007**, *127*, 194306.

[45] Granucci, G.; Persico, M.; Zoccante, A. Including quantum decoherence in surface hopping. *J. Chem. Phys.* **2010**, *133*, 134111.

[46] Subotnik, J. E. Fewest-switches hopping and decoherence in multiple dimensions. *J. Phys. Chem. A* **2011**, *115*, 12083–12096.

[47] Jaeger, H. M.; Fischer, S.; Prezhdo, O. V. Decoherence-induced surface hopping. *J. Chem. Phys.* **2012**, *137*, 22A545.

[48] Jasper, A. W.; Truhlar, D. G. Electronic decoherence time for non-Born–Oppenheimer trajectories. *J. Chem. Phys.* **2005**, *123*, 064103.

[49] Bonhommeau, D.; Valero, R.; Truhlar, D. G.; Jasper, A. W. Coupled-surface investigation of the photodissociation dynamics of NH3(A): Effect of exciting the symmetric and antisymmetric stretching modes. *J. Chem. Phys.* **2009**, *130*, 234303.

[50] Troe, J.; Ushakov, V. G. Anharmonic rovibrational numbers and densities of states for HO_2, H_2CO, and H_2O_2. *J. Phys. Chem. A* **2009**, *113*, 3940.

[51] Nguyen, T. L.; Barker, J. R. Sums and densities of fully coupled anharmonic vibrational states: A comparison of three practical models. *J. Phys. Chem. A* **2010**, *114*, 3718–3730.

[52] Kamarchik, E.; Jasper, A. W.; Anharmonic state counts and partition functions for molecules via classical phase space integrals in curvilinear coordinates. *J. Chem. Phys.* **2013**, *128*, 194109.

[53] Kamarchik, E.; Jasper, A. W. Anharmonic vibrational properties from intrinsic *n*-mode state densities. *Phys. Chem. Lett.* **2013**, *4*, 2430–2435.

[54] Jasper, A. W.; Nangia, S.; Zhu, C.; Truhlar, D. G. Non-Born–Oppenheimer molecular dynamics. *Acc. Chem. Res.* **2006**, *39*, 101–108.

[55] Tully, J. C. Molecular dynamics with electronic transitions. *J. Chem. Phys.* **1990**, *93*, 1061–1071.

[56] Jasper, A. W.; Stechmann, S. N.; Truhlar, D. G. Fewest-switches with time uncertainty: A modified trajectory surface-hopping algorithm with better accuracy for electronic transitions. *J. Chem. Phys.* **2002**, *116*, 5424–5431; **2002**, *117*, 10427(E).

[57] Meyer, H.-D.; Miller, W. H. A classical analog for electronic degrees of freedom in nonadiabatic collision processes. *J. Chem. Phys.* **1979**, *70*, 3214–3223.

[58] Zhu, C.; Jasper, A. W.; Truhlar, D. G. Non-Born–Oppenheimer trajectories with self-consistent decay of mixing. *J. Chem. Phys.* **2004**, *120*, 5543–5557.

[59] Jasper, A. W.; Truhlar, D. G. Conical intersections and semiclassical trajectories: Comparison of accurate quantum dynamics and analyses of the trajectories. *J. Chem. Phys.* **2005**, *112*, 044101.

[60] Maiti, B.; Schatz, G. C. Theoretical studies of intersystem crossing effects in the O(^{3}P, ^{1}D) + H_2 reaction. *J. Chem. Phys.* **2003**, *119*, 12360.

[61] Deskevich, M. P.; Nesbitt, D. J.; Werner, H. J. Dynamically weighted multiconfiguration self-consistent field: Multistate calculations for F + H_2O → HF + OH reaction paths. *J. Chem. Phys.* **2004**, *120*, 7281–7289.

[62] Dawes, R.; Jasper, A. W.; Tao, C.; Richmond, C.; Mukarakate, C.; Kable, S. H.; Reid, S. A. Theoretical and experimental spectroscopy of the S_2 state of CHF and CDF: Dynamically wighted multireference configuration interaction calculations for high-lying electronic states. *J. Phys. Chem. Lett.* 2010, *1*, 641–646.

[63] Berning, A.; Schweizer, M.; Werner, H.-J.; Knowles, P. J.; Palmier, P. Spin-orbit matrix elements for internally contracted multireference configuration interaction wavefunctions. *Mol. Phys.* **2000**, *98*, 1823–1833.

[64] Dawes, R.; Wagner, A. F.; Thompson, D. L. Ab initio wavenumber accurate spectroscopy: $^1CH_2$ and HCN vibrational levels on automatically generated IMLS potential energy surfaces. *J. Phys. Chem. A.* **2009**, *113*, 4709–4721.

[65] Dawes, R.; Thompson, D. L.; Wagner, A. F.; Minkoff, M. Interpolating moving least-squares methods for fitting potential energy surfaces: A strategy for efficient automatic point placement in high dimensions. *J. Chem. Phys.* **2008**, *128*, 084107.

[66] Miller, W. H. Unified statistical model for "complex" and "direct" reaction mechanisms. *J. Chem. Phys.* **1976**, *65*, 2216–2223.

[67] Klippenstein, S. J.; Khundkar, L. R.; Zewail, A. H.; Marcus, R. A. Application of unimolecular reaction rate theory for highly flexible transition states to the dissociation of NCNO into NC and NO. *J. Chem. Phys.* **1988**, *89*, 4761–4770.

[68] Jasper, A. W.; Pelzer, K. M.; Miller, J. A.; Kamarchik, E.; Harding, L. B.; Klippenstein, S. J. Predictive a priori pressure dependent kinetics. *Science*, **2015**, *346*, 1212–1215.

[69] Miller, J. A.; Klippenstein, S. J. Master equation methods in gas phase chemical kinetics. *J. Chem. Phys. A* **2006**, *110*, 10528–10544.

Table of contents graphic